PERGAMON

International Journal of Heat and Mass Transfer 42 (1999) 4501–4521

International Journal of HEAT and MASS TRANSFER

www.elsevier.com/locate/ijhmt

A 3-D version of TransPore: a comprehensive heat and mass transfer computational model for simulating the drying of porous media

Patrick Perré[a,*], Ian W. Turner[b]

[a]E.N.G.R.E.F., Laboratory of Forest Sciences, Forest Products Team, 14 rue Girardet, F-54042 Nancy Cedex, France
[b]School of Mathematical Sciences, Queensland University of Technology, GPO Box 2434, Brisbane, Q4001, Australia

Received 7 January 1999; accepted 15 March 1999

Abstract

The coupled and highly non-linear nature of the transport equations that govern the drying process highlights the applicability of numerical simulation in this field. This work is devoted to presenting the latest version of TransPore: a unique 3-D drying model that is able to deal with the heat and mass transfer in porous media. The set of equations used in the present work is among the more comprehensive physical descriptions for the drying of a porous medium modelled at the macroscopic scale.

Several simulation results are presented that depict the new possibilities offered by such a tool. In particular, the effect of the number of exchange faces is studied both for an isotropic medium (a cube of light concrete) and for an anisotropic medium (a board of wood) where the anisotropy ratios and geometrical factors are large. These simulations prove that only three spatial dimensions are able to capture the effect of the width of the medium in the case of high temperature drying. Indeed, with such conditions, the longitudinal direction is required to highlight the effect of overpressure in a strongly anisotropic medium, while both thickness and width are necessary to account for the coupling between the thermal field and the pressure driven flow. © 1999 Published by Elsevier Science Ltd. All rights reserved.

1. Introduction

In this work a new three-dimensional (3-D) drying model is presented. Three macroscopic state variables (one for the energy conservation equation, one for the moisture conservation and one for the conservation of the gaseous phase) are used to describe the drying process. The most important physical phenomena treated in the formulation include capillary and convective liquid flow, bound and gaseous diffusion and convective gaseous migration, thermal conductivity and heat required for evaporation. Finally, isotherm curves, heat and mass exchange terms, and conditions on full saturation [17] allow the closure of this system.

The resulting code is quite complex and can be time consuming in terms of CPU time for the large meshes encountered with three spatial dimensions. In order to counterbalance this effect, state-of-the-art numerical techniques such as quasi-Newton methods for solving the non-linear discrete network and pre-conditioned conjugate gradient solvers for resolving the linearised sparse matrix system are employed.

To date a number of comprehensive two-dimensional (2-D) models are available for studying the drying process. These models have been applied in the domains of wood drying [9,10,6,3] and building materials, such as brick [2]. These models have provided

* Corresponding author.

0017-9310/99/$ - see front matter © 1999 Published by Elsevier Science Ltd. All rights reserved.
PII: S0017-9310(99)00098-8

the drying engineer with fundamental knowledge that has increased the understanding of the process and allowed new and innovative drying operations to be proposed.

The motivation for developing a 3-D model for drying originates from the conclusions drawn from some of the previous 2-D studies carried out by the authors. Firstly, drying stresses that develop in wood during drying depend strongly on the board width [8], while the longitudinal direction is important to represent transport phenomena. Secondly, such a model is absolutely necessary before a comprehensive radio frequency or microwave drying simulation can be performed [11].

The use of three spatial dimensions in porous media modelling is not new, however, to our knowledge, comprehensive computation models do not exist currently in the field of drying research. Some simple transfer models exist for studying the absorption and desorption of water in a wood beam [7] and for analysing moisture distortion modelling of wood and structural timber [13], however, a complete resolution of the coupled and highly non-linear drying model equations appears to be a new contribution to the literature. In the fields of ground water flow, petroleum reservoir simulation and pollution modelling one can find a wealth of references pertaining to 3-D models implemented on both structured and unstructured meshes [1,4,20,5,15]. It is clear from all of the above studies that although in principle it appears straightforward to pass from two spatial dimensions to three, some rather subtle numerical analysis and innovative concepts in linear algebra are required if efficient computation times for the simulations are to be realised.

In this work two case studies have been chosen to test the performance of the 3-D model. In Case Study 1, the high temperature convective drying of light concrete is presented, while in Case Study 2, the results for both low and high temperature convective drying of softwood are analysed. In particular, it will be shown that only three spatial dimensions are able to capture the correct physical behaviour of the porous medium throughout the drying process. Indeed, high temperature drying induces an important overpressure in the longitudinal direction of the board that is a trademark of a highly anisotropic porous medium. The thickness and width of the board are necessary to account for the coupled mechanisms of thermal and mass diffusion, and Darcy's flow.

2. Mathematical formulation

In this section of the paper the drying conservation equations, together with the relevant flux expressions and constitutive relations will be presented. The discretisation process will be analysed and the numerical solution procedure will be outlined briefly. Some specific computation details for the new 3-D model will be discussed.

2.1. The transport model

Whitaker [18,19] has discussed the macroscopic equations that govern heat and mass transfer phenomena in porous media in detail. These equations have been used subsequently to model the softwood drying process [9,21,10], where their ability to describe several different drying configurations has been proven. These equations are summarised as follows:

Liquid conservation

$$\frac{\partial}{\partial t}(\varepsilon_w\rho_w + \varepsilon_g\rho_v + \bar{\rho}_b) + \nabla\cdot(\rho_w\bar{\mathbf{v}}_w + \rho_v\bar{\mathbf{v}}_g + \overline{\rho_b\mathbf{v}_b}) = \nabla\cdot(\rho_g\overline{\overline{\mathbf{D}}}_{\text{eff}}\nabla\omega_v) \tag{1}$$

Energy conservation

$$\frac{\partial}{\partial t}(\varepsilon_w\rho_w h_w + \varepsilon_g(\rho_v h_v + \rho_a h_a) + \bar{\rho}_b\bar{h}_b + \rho_0 h_s - \varepsilon_g P_g) + \nabla\cdot(\rho_w h_w\bar{\mathbf{v}}_w + (\rho_v h_v + \rho_a h_a)\bar{\mathbf{v}}_g + h_b\overline{\rho_b\mathbf{v}_b}) = \nabla\cdot(\rho_g\overline{\overline{\mathbf{D}}}_{\text{eff}}(h_v\nabla\omega_v + h_a\nabla\omega_a) + \overline{\overline{\mathbf{K}}}_{\text{eff}}\nabla T) + \Phi \tag{2}$$

Air conservation

$$\frac{\partial}{\partial t}(\varepsilon_g\rho_a) + \nabla\cdot(\rho_a\bar{\mathbf{v}}_g) = \nabla\cdot(\rho_g\overline{\overline{\mathbf{D}}}_{\text{eff}}\nabla\omega_a) \tag{3}$$

where the gas and liquid phase velocities are given by the Generalised Darcy's Law:

$$\bar{\mathbf{v}}_l = -\frac{\overline{\overline{\mathbf{K}}}_l\overline{\overline{\mathbf{k}}}_l}{\mu_l}\nabla\varphi_l, \quad \nabla\varphi_l = \nabla P_l - \rho_l g\nabla\chi \quad \text{where} \quad l = w, g \tag{4}$$

The quantities φ are known as the phase potentials and χ is the depth scalar. All other symbols have their usual meaning.

2.2. Boundary and initial conditions

There are two types of boundary conditions that need to be discussed, namely, conditions at external boundaries and conditions at symmetry planes. The boundary conditions proposed for the external drying

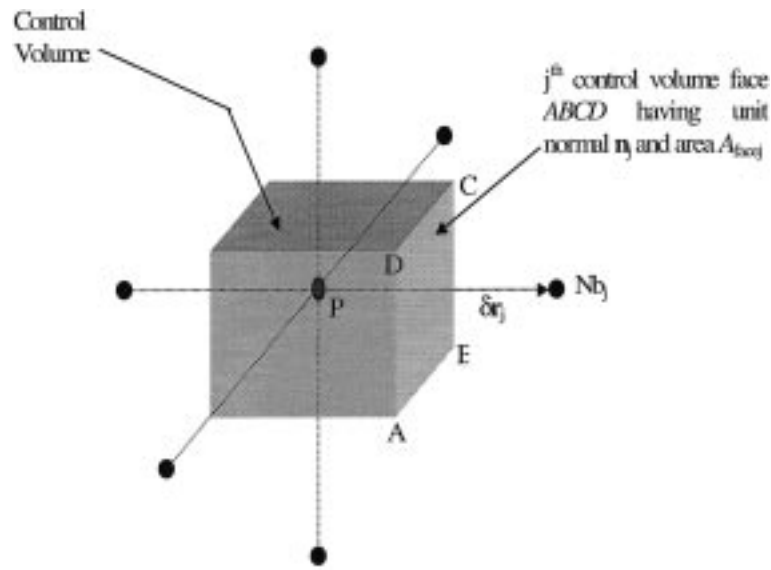

Fig. 1. 3-D hexahedral control volume used for the discretisation process.

surfaces of the sample are assumed to be of the following form (see [10]):

$$\mathbf{J}_w \cdot \hat{\mathbf{n}} = k_m c M_v \ \ln\left(\frac{1-x_\infty}{1-x_v}\right)$$

$$\mathbf{J}_e \cdot \hat{\mathbf{n}} = q(T-T_\infty) + h_v k_m c M_v \ \ln\left(\frac{1-x_\infty}{1-x_v}\right) \tag{5}$$

where $\mathbf{J}_w$ and $\mathbf{J}_e$ represent the fluxes of total moisture and total enthalpy at the boundary, respectively. The pressure at the external drying surfaces is fixed at the atmospheric value. Recalling that one of the primary variables used for the computations is the averaged air density, the Dirichlet boundary condition $P_g = P_\infty$ has to be modified to form an appropriate non-linear equation for this primary variable:

$$\varepsilon_g(P_v - P_\infty) + \frac{\bar{\rho}_a RT}{M_a} = 0 \tag{6}$$

Eq. (6) must be resolved, along with the conservation laws, during the non-linear iterations for every external boundary control volume within the computational domain.

Symmetry planes are introduced into the model to reduce the overall computation times. For the porous sample under consideration here, only one eighth of the sample is computed and all fluxes of liquid, vapour, air and heat are assumed zero at the symmetry planes. Initially the porous medium has some prescribed moisture and temperature distribution, with the pressure being constant throughout at the atmospheric value.

2.3. Numerical strategies used for the resolution of the transport model

In order to illustrate the discretisation process, it has been decided for the sake of clarity to analyse only the liquid conservation law (1). The overall procedure is identical for the other two conservation laws. The discretisation process proceeds by integrating the balance law over a typical hexahedral control volume of the form exhibited in Fig. 1.

After integrating over each control volume within the computational domain, a system of non-linear equations results whereby each equation within this system can be cast into a discrete analog of the conservation equation, for example:

$$\begin{aligned} F_w(\mathbf{u}_p) &\equiv \frac{\Delta V_p}{\delta t}(\psi_{w_p}^{n+1} - \psi_{w_p}^{n}) \\ &\quad - \sum_{i \in Nb_p} (\mathbf{J}_w \cdot \hat{\mathbf{n}})_{CV_{\text{face}_i}} A_{\text{face}_i} = 0, \\ \mathbf{J}_w &= \overline{\overline{\mathbf{K}}}_w \overline{\overline{\lambda}}_w \rho_w \nabla \varphi_w + \overline{\overline{\mathbf{K}}}_g \overline{\overline{\lambda}}_g \rho_v \nabla \varphi_g + \overline{\overline{\mathbf{D}}}_{\text{eff}} \rho_g \nabla \omega_v \\ &\quad + \overline{\overline{\mathbf{D}}}_b \nabla \mu_b \end{aligned} \tag{7}$$

In Eq. (7) the term ψ_w represents the conserved quantity of total liquid: $\psi_w = \varepsilon_w \rho_w + \varepsilon_g \rho_v + \bar{\rho}_b$. Nb_p denotes the set of neighbouring points that surround the node $\mathbf{p}$. The tensor terms in this equation [absolute permeabilities $\overline{\overline{\mathbf{K}}}$, mobilities $\overline{\overline{\lambda}} = (\overline{\overline{\mathbf{k}}}/\mu)$ and diffusivities $\overline{\overline{\mathbf{D}}}$] within the flux expression are functions of the state system variables. Because Eq. (7) requires expressions for the discrete form of the flux in the normal direction

to the CV face, it is necessary to approximate all of the gradient terms. For an orthogonal mesh, the gradient of given quantity ϕ can be approximated simply as $(\nabla\phi)_{CV_{\text{face}i}} = [(\phi_{nb_i} - \phi_p)/\|\delta\mathbf{r}_i\|]\delta\hat{\mathbf{r}}_i$ (see [16]). However, it should be noted that this formula needs to be modified if the mesh is non-orthogonal, in which case a correction term for the tangential component of the gradient must be added. Nevertheless, by substituting this expression where appropriate into (7), the following discrete form of the flux results:

$$
\begin{aligned}
&(\mathbf{J}_w \times \mathbf{n})_{CV_{\text{face}_i}} \\
&\quad = \delta\hat{\mathbf{r}}_i^T(\bar{\bar{\lambda}}_w)_{CV_{\text{face}_i}} \cdot \bar{\gamma}_{w_i}(\rho_w)_{CV_{\text{face}_i}}(\varphi_{w_{nb_i}} - \varphi_{w_p}) \\
&\qquad + \delta\hat{\mathbf{r}}_i^T(\bar{\bar{\lambda}}_g)_{CV_{\text{face}_i}} \cdot \bar{\gamma}_{g_i}(\rho_v)_{CV_{\text{face}_i}}(\varphi_{g_{nb_i}} - \varphi_{g_p}) \\
&\qquad + \delta\hat{\mathbf{r}}_i^T(\bar{\bar{\mathbf{D}}}_b)_{CV_{\text{face}_i}} \cdot \bar{\gamma}_{b_i}(\mu_{b_{nb_i}} - \mu_{b_p}) \\
&\qquad + \delta\mathbf{r}_i^T(\bar{\bar{\mathbf{D}}}_{\text{eff}})_{CV_{\text{face}_i}} \cdot \bar{\gamma}_{v_i}(\rho_g)_{CV_{\text{face}_i}}(\omega_{v_{nb_i}} - \omega_{v_p})
\end{aligned}
\tag{8}
$$

where it has been assumed that the tensor terms are diagonal. This assumption is reasonable when the anisotropy of the system is taken to be in the direction of the principal axes of a Cartesian co-ordinate system. The more complication configuration, where the material axes are rotated according to the position from which the board is cut from the tree, has been discussed in detail elsewhere [12]. The vector quantities $\bar{\gamma}_i$ represent geometric quantities, where for example, $\bar{\gamma}_{w_i} = (\bar{\bar{\mathbf{K}}}_w\mathbf{n}_i/\|\delta\mathbf{r}_i\|)$, and an efficient way of computing the normal for each control volume face is to use (referring to Fig. 1 and face $ABCD$) $\mathbf{n} = \frac{1}{2}(\mathbf{x}_{AC} \times \mathbf{x}_{BD})$. Note that a term like $(\bar{\bar{\lambda}}_w)_{CV_{\text{face}_i}}$ implies evaluation of the components of the liquid mobility tensor at the ith CV face.

The discrete analogue (7) of the liquid conservation law (1) is a complication non-linear function of the state variable set (S_w, P_w, T, $\bar{\rho}_a$, ρ_v, $\bar{\rho}_b$) at the nodes $\mathbf{p}$ and all of the neighbouring nodes that surround the control volume (CV_p) under consideration. The coefficients within expression (8) combine the non-linearities of the transport coefficients, which involve the state function set at the node $\mathbf{p}$ and the neighbouring node $\mathbf{nb}_i$, together with the relevant geometric factors for the control volume face. Note that the advection transport coefficients must be treated differently from the diffusive terms otherwise the solutions may not be monotonic.

For each CV, the state variable set is assumed to have an exact definition. In fact, out of this six variable set only three variables, known as the primary variables, will be treated as the unknown independent variables for each CV and the remaining three variables, known as secondary variables, will be computed according to the values of these primary variables. The values of all variables are presumed known at the nth time level. Once the non-linear functions are assembled for each CV within the computation domain, the result is a system of non-linear equations of the form $\mathscr{F}(\mathbf{u}) = \mathbf{0}$. The solution vector $\mathbf{u}$ contains the primary variables (in triplets) for each CV within the mesh. This system must be resolved, at each time step, in order to advance all of the primary variables in time.

The solution procedure is carried out in two distinct stages via what are known as outer and inner iteration phases. During the outer iteration phase, the system of non-linear equations is linearised according to a quasi-Newton scheme. The estimate of the solution vector at the $(n+1)$th level is computed from the current solution at the nth level by writing

$$\mathbf{u}^{(n+1)} = \mathbf{u}^{(n)} + \delta\mathbf{u}^{(n)} \tag{9}$$

and solving the system of linearised equations

$$\mathbf{B}(\mathbf{u}^{(n)})\delta\mathbf{u}^{(n)} = -F(\mathbf{u}^{(n)}) \tag{10}$$

for the correction vector $\delta\mathbf{u}^{(n)}$. In Eq. (10), $\mathbf{B}$ represents an approximation to the true Jacobian matrix. The exact approximation used for $\mathbf{B}$ will be the subject of an article that is being compiled currently by the authors. Nevertheless, it suffices to say that the derivatives needed for the construction of the Jacobian are computed numerically using simple finite difference approximations [16] that seek to balance the need for excessive (and expensive) function evaluations against the order of the approximation.

To illustrate this strategy, assume that Eq. (7) can be written in the following form:

$$
\begin{aligned}
F_w(\mathbf{u}_p) \equiv\ & (\Psi_w(\mathbf{u}_p^{(n+1)}) - \Psi(\mathbf{u}_p^{(n)})) \\
& - \sum_{i \in Nb_p} \text{Flux}(\mathbf{u}_p^{(n+1)}, \mathbf{u}_{nb_i}^{(n+1)}) = 0
\end{aligned}
\tag{11}
$$

where, for example,

$$\Psi(\mathbf{u}_p^{(n+1)}) = \frac{\Delta V_p}{\delta t}\psi_{w_p}^{n+1} \quad \text{and}$$

$$\mathbf{u}_p^{(n+1)} = (X_p^{(n+1)}, \tilde{T}_p^{(n+1)}, \bar{\rho}_{a_p}^{(n+1)})^T, \quad X = \frac{(\varepsilon_w\rho_w + \bar{\rho}_b)}{\rho_0}$$

is the moisture content and $\tilde{T}$ represents the non-dimensional temperature. The derivative of $F_w(\mathbf{u}_p)$ with respect to X_p can be computed using the following expression:

$$\frac{\partial F_w}{\partial X_p} \approx \frac{(\Psi(\mathbf{u}_p^*) - \Psi(\mathbf{u}_p))}{\varepsilon} - \sum_{i \in Nb_p} \frac{(\mathrm{Flux}(\mathbf{u}_p^*, \mathbf{u}_{nb_i}) - \mathrm{Flux}(\mathbf{u}_p, \mathbf{u}_{nb_i}))}{\varepsilon} \tag{12}$$

where $\mathbf{u}_p^* = (X_p + \varepsilon, \tilde{T}_p, \bar{\rho}_{a_p})^{\mathrm{T}}$ and ε is a suitably chosen numerical shift value that must be chosen large enough to avoid roundoff errors and small enough to elude a poor approximation for the derivative. Assuming that the primary variables are all non-dimensionalised to be $O(1)$, then a useful rule of thumb is to compute the shift factor used in (12) according to the square root of the unit roundoff. We have used values of $\varepsilon = 10^{-7}$ and have always been able to observe quadratic convergence of the Newton scheme.

The Jacobian matrix (or its approximation) has a sparse structure, and due to its condition, must be solved with a great deal of care iteratively. In this work, during the inner iteration phase, system (10) is solved by employing the Bi-Conjugate Gradient Stabilised Method [22], together with an Incomplete Factorisation level zero, $ILU(0)$, preconditioning technique. Another factor that is important to the performance of the convergence of the iterative solver, and in particular the pre-conditioner, concerns the ordering of the nodes within the solution domain. Obviously, if an LU decomposition procedure is going to be used as the pre-conditioner one must take care to minimise the band-width of the sparse matrix. Such a minimisation can be achieved using the Reverse Cuthill–McKee algorithm.

2.4. Evaluation of the tensor terms at the CV face

As can be seen from Eq. (8), it is necessary to define spatial averaging technique for the evaluation of the tensor terms at the control volume faces. Typically, diffusion terms are averaged using either arithmetic or harmonic averaging strategies. Referring again to Fig. 1, and defining the interpolation factors:

$$\delta r_i^- = \frac{\|\delta \mathbf{r}_i^-\|}{\|\delta \mathbf{r}_i\|}, \quad \delta r_i^+ = \frac{\|\delta \mathbf{r}_i^+\|}{\|\mathbf{r}_i\|}$$

the components of the diffusion tensors $\overline{\overline{\mathbf{D}}}_{\mathrm{eff}}$ and $\overline{\overline{\mathbf{D}}}_b$ are averaged using the following arithmetic averaging strategy:

$$d_{jk_{CV_{\mathrm{face}_i}}} = \delta r_i^+ d_{jk_p} + \delta r_i^- d_{jk_{nb_i}}$$

The correct treatment of the advection and convection terms is essential to the accuracy and performance of the numerical scheme. In this work upstream weighting, which is a first-order spatial averaging method that is known to converge to the physically correct solution [14], has been adopted:

$$(\overline{\overline{\lambda}})_{ups(p,nb_i)} = \begin{cases} \overline{\overline{\lambda}}_p & \text{if } (\mathbf{v} \cdot \mathbf{n}) \geq 0 \\ \overline{\overline{\lambda}}_{nb_i} & \text{if } (\mathbf{v} \cdot \mathbf{n}) < 0 \end{cases} \tag{13}$$

3. Results and discussion

This section is devoted to presenting the simulation results obtained from the computational model proposed above. The purpose of this study is to use the simulation results to elucidate upon the 3-D coupled mechanisms that take place during drying. It is hoped that the simulation possibilities offered by this new 3-D tool will be highlighted throughout the discussion that follows. Results are presented for two different configurations, ranging from a cube of an isotropic material (light concrete) to a long sample of a strongly anisotropic material (softwood) dried at high temperature. In the case of wood, because special attention is paid to the effect of the board width, which is the main improvement compared to the existing 2-D version of TransPore, three boards of different dimensions have been chosen and subsequently meshed:

- 1 m × 3 cm × 3 cm (L-, R- and T-directions, respectively);
- 1 m × 6 cm × 3 cm (L-, R- and T-directions, respectively);
- 1 m × 12 cm × 3 cm (L-, R- and T-directions, respectively).

For all configurations, the presence of three symmetry planes allows the code to deal only with one eighth of the sample. Moreover, in order to save computation time, the mesh is refined close to the exchange surfaces, where the variable gradients are likely to be the most important. The geometrical factors are chosen so that the corner control volume (0, 0, 0 for X-, Y- and Z-coordinates) is almost a cube, whatever the aspect ratio of the sample. Three mesh examples are exhibited in Fig. 2. The grids used in the present work are rather coarse (20 × 15 × 10 in the L-, R- and T-direction for the 12 cm thick board), however, they are sufficient to capture all of the physical phenomena that transpire during the drying process. Supporting evidence of this fact can be found throughout the numerous studies carried out in 2-D by the authors [9,21,16].

3.1. High temperature convective drying in a cube of an isotropic medium

A very simple configuration is used for the first application of the 3-D version of TransPore: a cube of light concrete (an isotropic medium) is dried by a con-

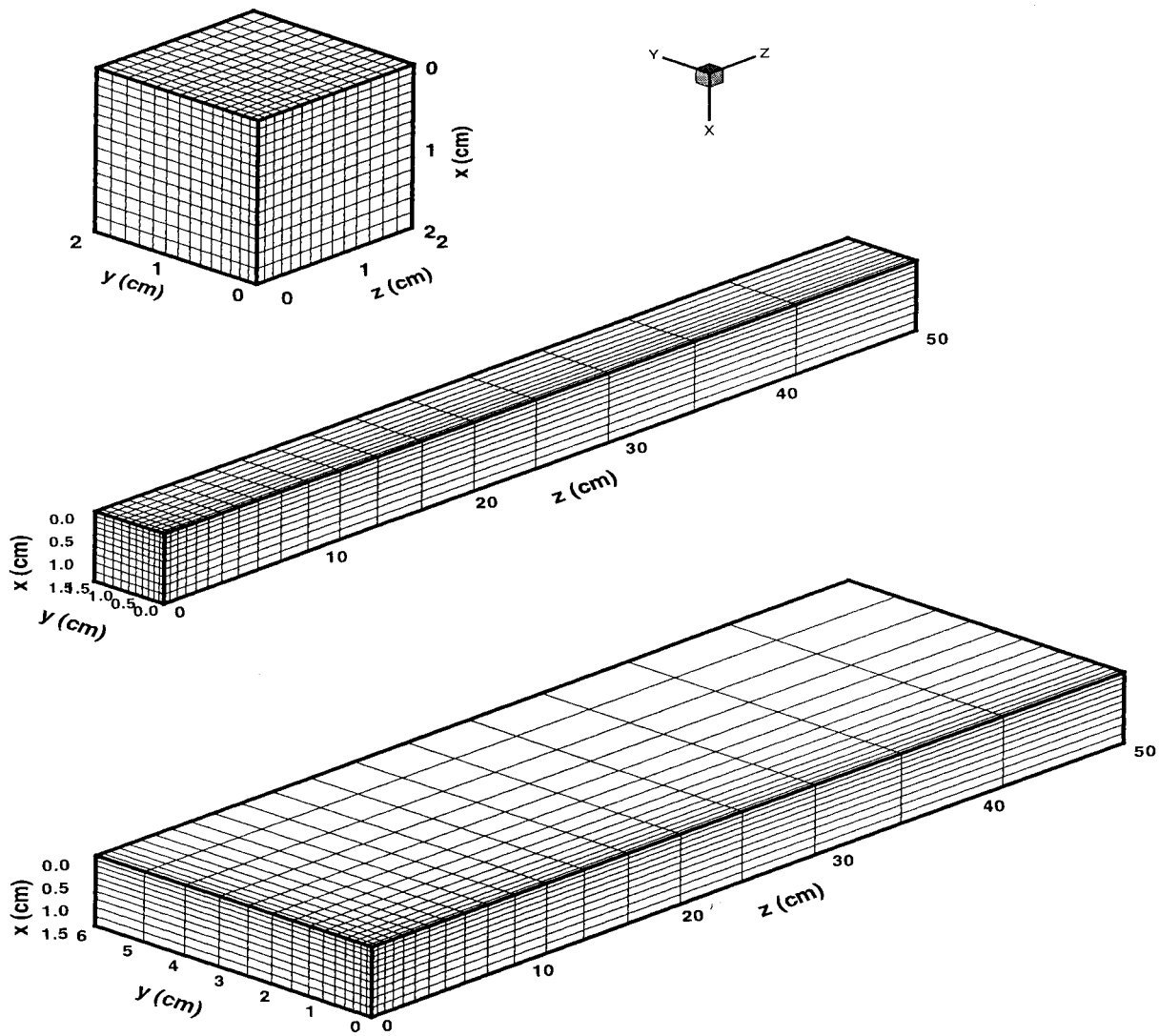

Fig. 2. Three mesh examples: note the mesh refinement around the exchange surfaces: 1/8 of 4 × 4 × 4 cm cube of concrete, 1/8 of a 3 × 3 × 50 cm board, 1/8 of a 3 × 12 × 50 cm board.

vective air flow (dry bulb temperature = 140°C, dew point = 80°C).

Fig. 3 represents the computed variable isosurfaces at 2 h of drying. The presence of three orthogonal exchange faces forces the moisture content to be very low at the corner. At that drying time, only the core of the cube retains a high value of moisture content. The temperature and pressure fields allow more subtle phenomena to be observed. The temperature varies significantly in space only in the region of vapour migration (vapour diffusion and most importantly, gaseous Darcy's flow). In this region, the temperature gradient is required to supply the energy necessary for allowing the liquid to change phase to vapour. The pressure gradient that exists in this zone results from a cross diffusion effect of vapour and air. The bulk flow induced by Darcy's law applied to the gaseous phase keeps the total air flux almost equal to zero. This phenomenon explains why the only two pressure isovalues that have been plotted are close to the exchange surfaces. Almost no pressure gradient exists in the domain of free water.

In order to exhibit clearly the effect of tri-dimensional transfers, two other simulations have been performed on the same geometry and for the same drying conditions, however, using a different number of

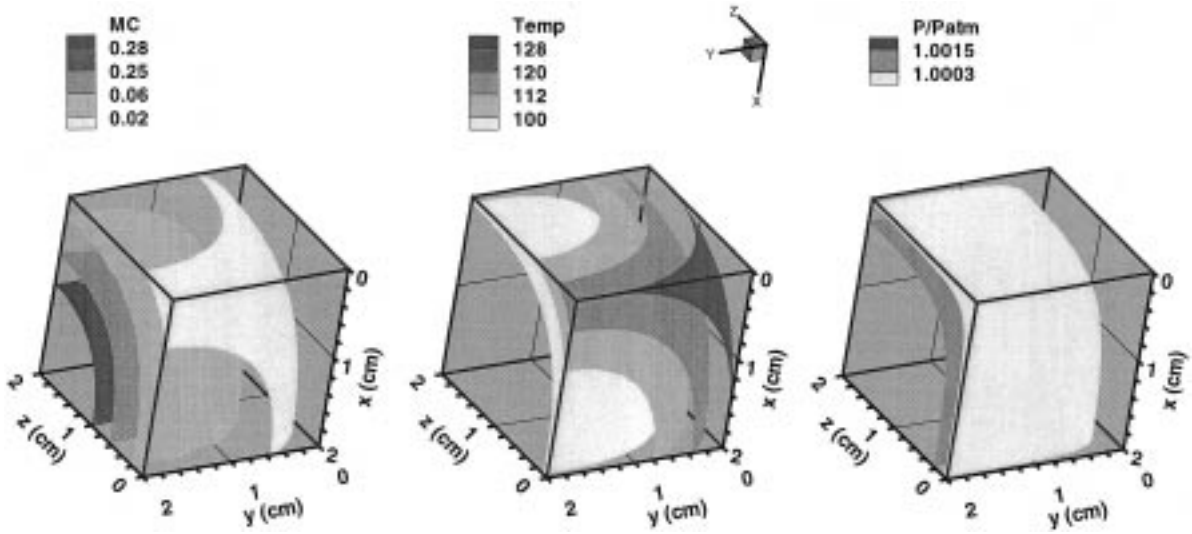

Fig. 3. Numerical simulation of concrete drying (140/80°C for dry and wet bulbs, respectively). 3-D variable fields calculated at 2 h or drying.

exchange faces. This strategy allowed 1-, 2- and 3-D transfer mechanisms to be compared directly. The evolution in time of average moisture content, centre temperature and centre pressure is depicted in Fig. 4. From the evolution of the curves, the effect of the number of exchange surfaces on the process duration can be quantified. It is interesting to note that the drying time is almost proportional to the number of exchange surfaces, where by in comparison to the 1-D case, the drying time is about one half with two exchange surfaces and one third with three exchange surfaces.

Obviously, such a simple rule results from the equivalent role of each direction: cubic geometry, same exchange conditions and an isotropic medium. Note that, apart from the drying time, all physical mechanisms are alike. No fundamental changes in the drying behaviour can be observed. In particular, the maximum value of the overpressure is the same and, after the constant drying rate period, a plateau at around 85 to 90°C can be observed for all runs. This plateau is typical of light concrete: it results from a dynamic balance that exists between heat transfer and vapour flux (diffusion and bulk flow). It has been observed during experiments and has been explained by an analytical model [21].

3.2. Low temperature convective drying of a board of softwood

Convective drying of softwood is the second configuration that has been chose to test the code. Compared to the first test, the material is now highly anisotropic and the sample shape involves important geometrical factors (1 m × 12 cm × 3 cm in the *L*-, *R*- and *T*-directions). The drying fluid is moist air, with a dry bulb temperature below the boiling point of water (dry bulb temperature = 80°C, dew point = 50°C, heat transfer coefficient = 25 W m^{-2} °C^{-1}).

Since 3-D results are not particularly easy to plot and analyse, it was decided to illustrate the coupling between the three state variables by drawing 'fence plots' at different drying times. This allows the spatial field to be reconstructed by interpolating (by mind) the isovalues at regular board sections, together with the isovalues plotted over the three planes of symmetry. Because the computed mesh is not regularly spaced, these sections have to be calculated by linear interpolation.

Figs. 5–7 depict the 3-D fields of moisture content, temperature and dimensionless pressure at certain important drying stages, namely:

- 5 min: transient heating period;
- 4 h: transition between the constant drying rate period and the decreasing drying rate period;
- 30 h: end of the drying process.

After 5 min of drying, the temperature field is obviously non-uniform. The initial temperature of the board (30°C) is far below the dew point temperature. Consequently, the exchange faces are heated both by convective heat transfer and by the latent heat associated with the vapour that condenses at the surface. The core of the sample resembles the initial temperature field, however, the hottest zones of the sample are

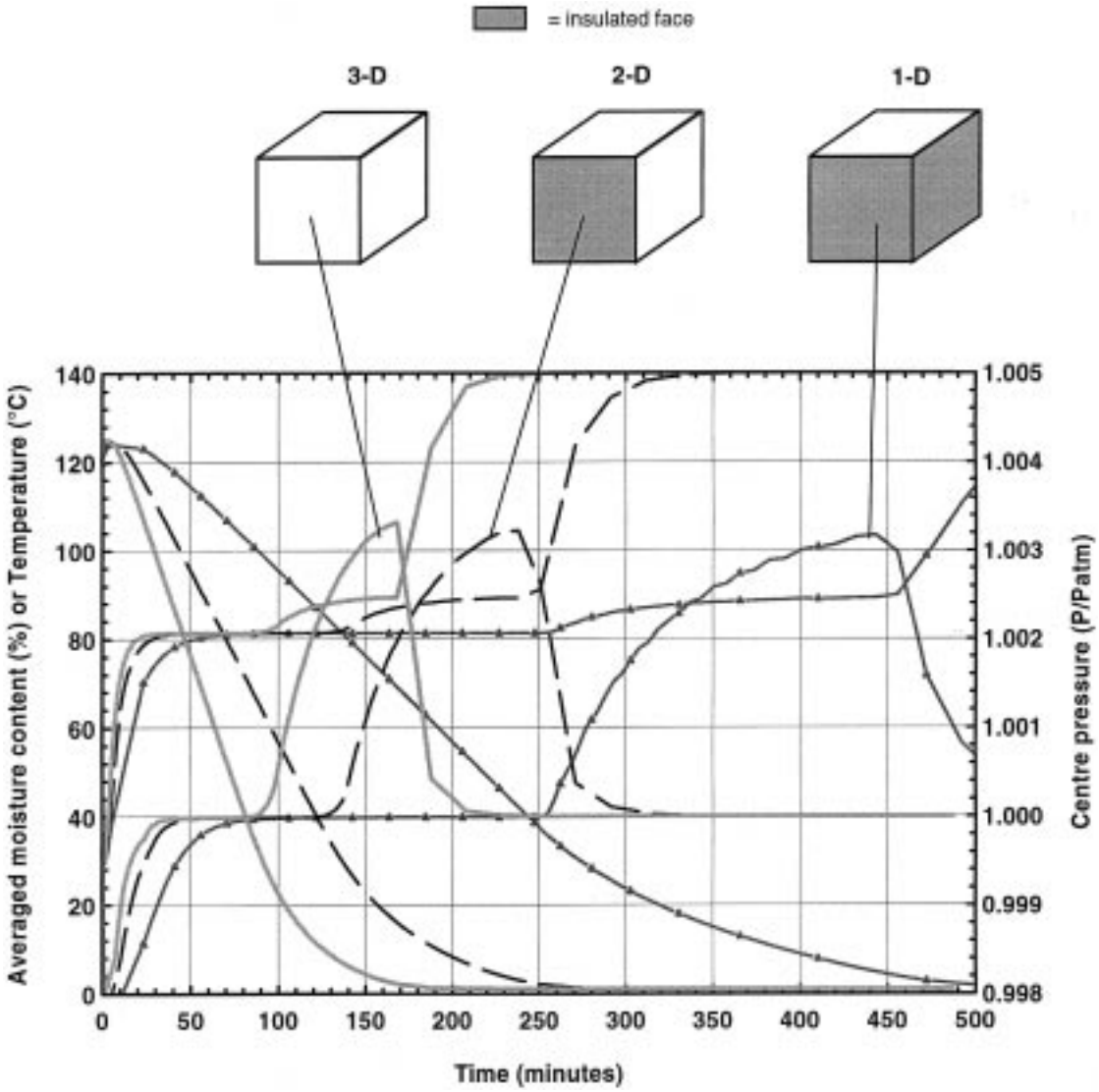

Fig. 4. Numerical simulation of concrete drying (140/80°C for dry and wet bulbs, respectively). Effect of the number of space dimensions on overall drying curves.

close to the intercept between two or three adjacent exchange faces (edge and corner of the board).

The moisture content field results from several phenomena:

- surface condensation;
- drying that already started in the hottest regions;
- longitudinal migration that has driven the condensation flux efficiently towards the inner part of the sample from the end piece.

Due to the sudden increase of temperature, the pressure also increased within the sample. Note that the Dirichlet boundary condition prevents the pressure from increasing in the vicinity of the exchange faces, especially along the longitudinal direction due to the high value of the permeability.

After 4 h of drying, the process is well established. The moisture content field results from the external exchange, together with the possibilities of internal transfer. Again, the presence of three exchange faces as well as the effect of material anisotropy can be observed from this moisture field. One can distinguish two different zones:

- the edge of the board is already within the hygroscopic domain. Consequently, the vapour pressure

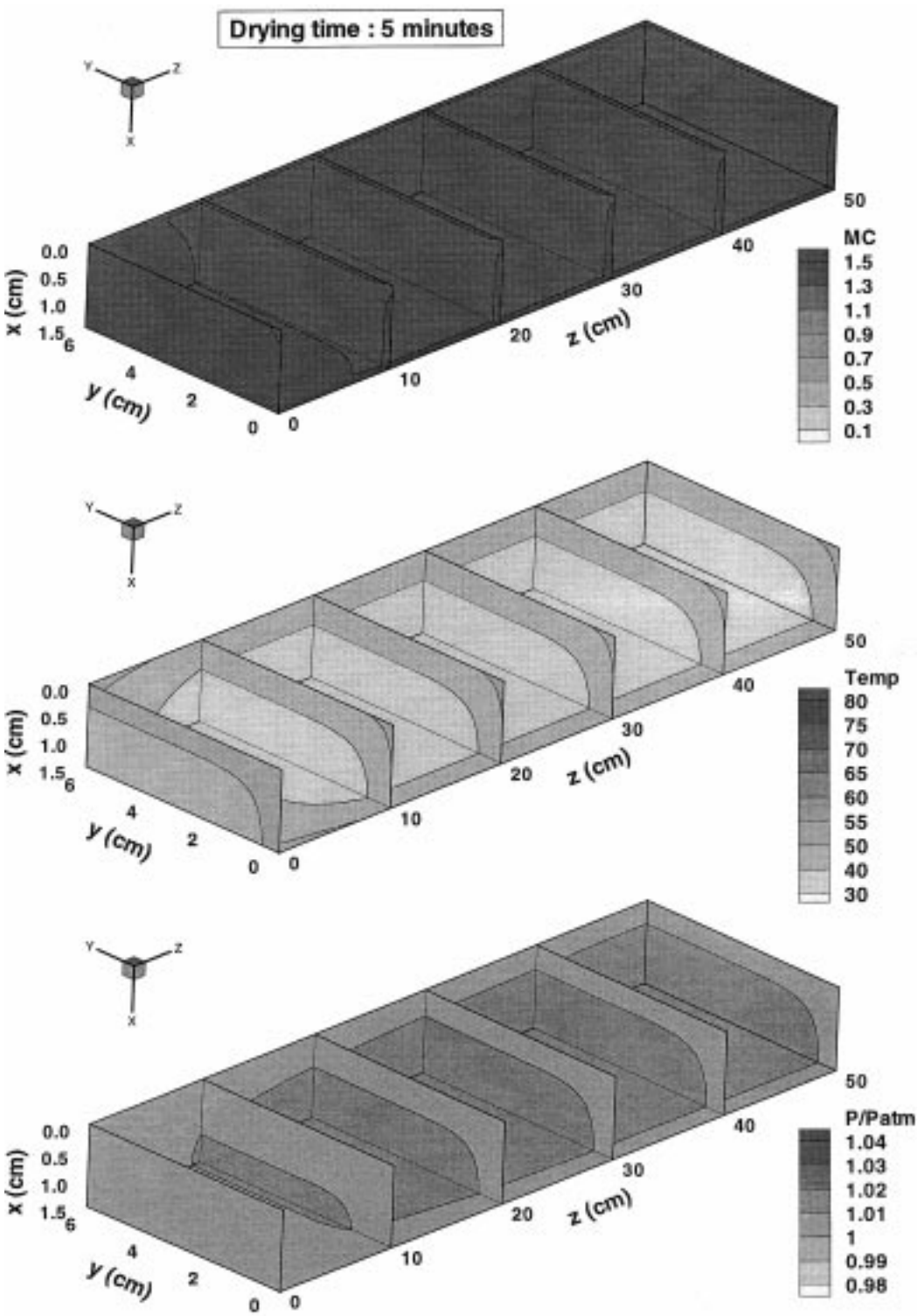

Fig. 5. Low temperature drying of softwood ($T_{dry} = 80°C$, $T_{wet} = 50°C$). Fence plot of moisture content, temperature and dimensionless pressure at 5 min of drying.

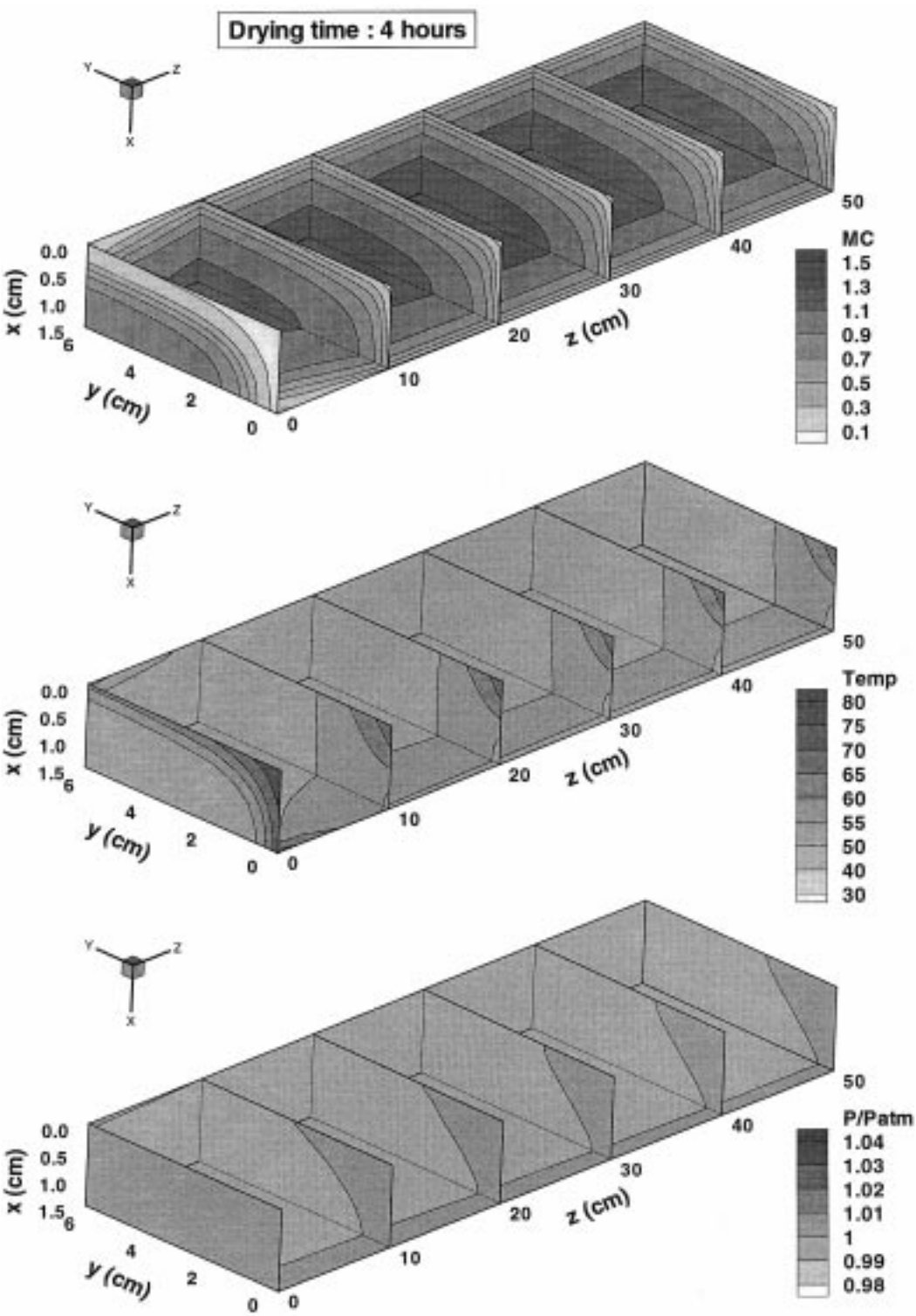

Fig. 6. Low temperature drying of softwood ($T_{dry} = 80°C$, $T_{wet} = 50°C$). Fence plot of moisture content, temperature and dimensionless pressure at 4 h of drying.

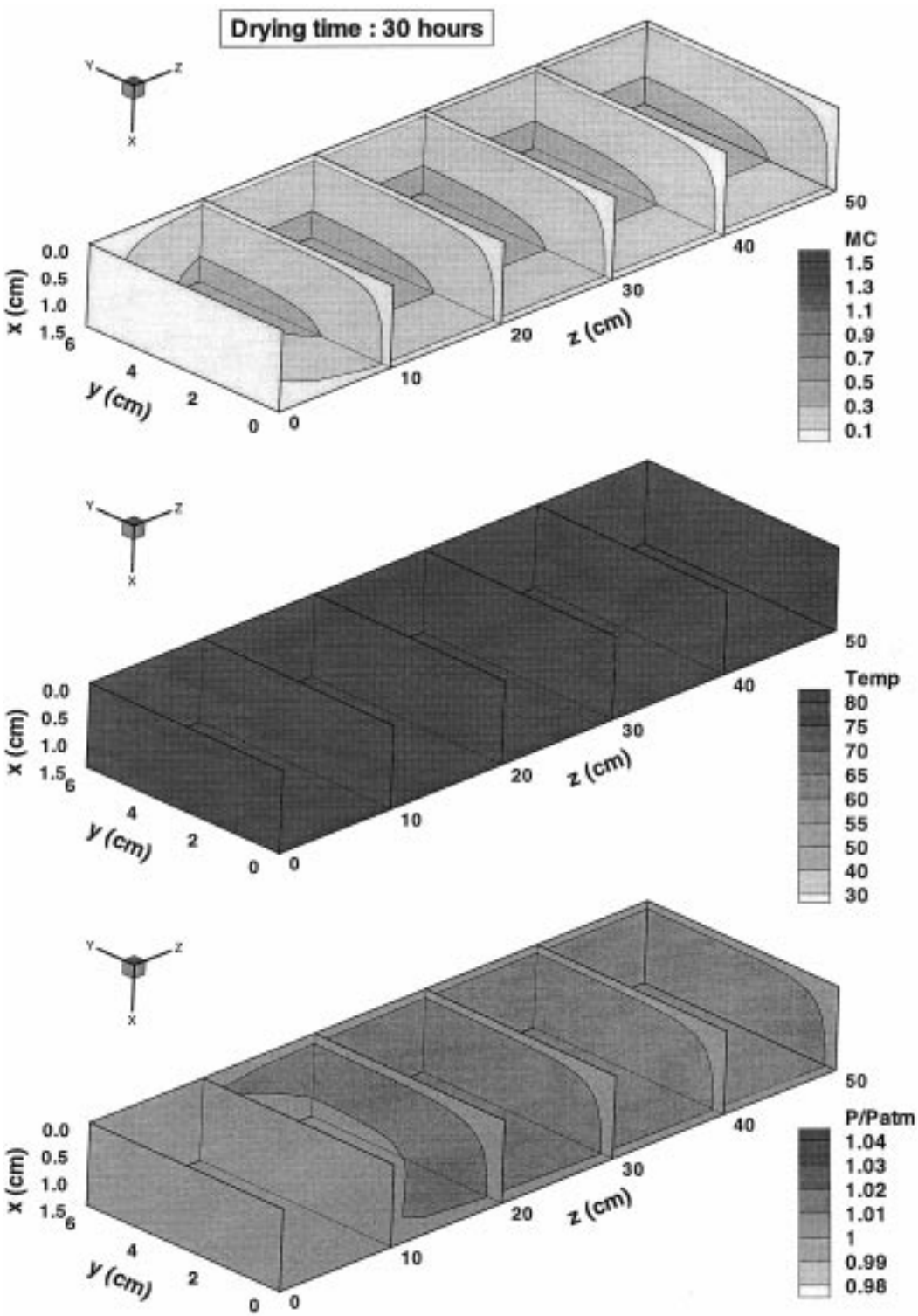

Fig. 7. Low temperature drying of softwood ($T_{dry} = 80°C$, $T_{wet} = 50°C$). Fence plot of moisture content, temperature and dimensionless pressure at 30 h of drying.

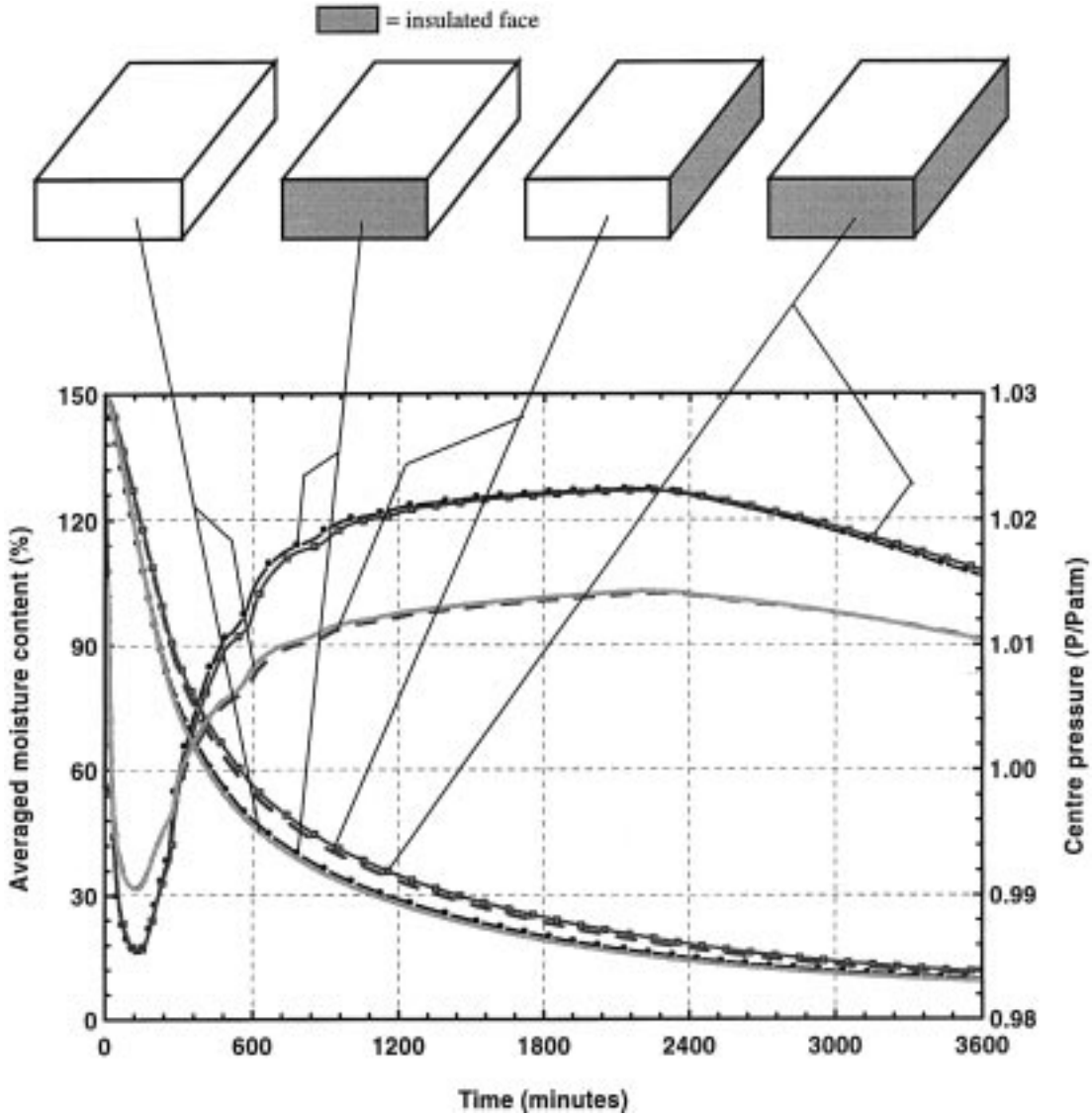

Fig. 8. Low temperature drying of softwood ($T_{dry} = 80°C$, $T_{wet} = 50°C$). Overall drying curve and internal pressure for different configurations of exchange surfaces.

at the surface is less than the saturated vapour pressure, which leads to an increase of temperature;

- the whole zone close to the half-width has its surface still in the domain of free water. This part of the board is driven by the mechanisms typical of the constant drying rate period, with the temperature resting at the wet bulb value and the mass flux being almost constant.

The corresponding zones can also be seen in the temperature and pressure fields. Note the underpressure in the zone that is still at the wet bulb temperature. This is consistent to the physical equation (increase of gaseous volume at constant temperature) and has been reported several times in previous works [9,10].

It is very interesting to notice that the first drying period reported by the global drying rate is seldom exactly constant on experimental curves. The smooth transition between the first and second drying periods, which can only be accounted for with 3-D calculations, procures more realistic drying curves. This may be particularly important when proceeding to comparison between theory and experiment.

Finally, at 30 hours of drying, the process is almost at its end. Some residual moisture and a slight overpressure must be noted in the core of the sample. The

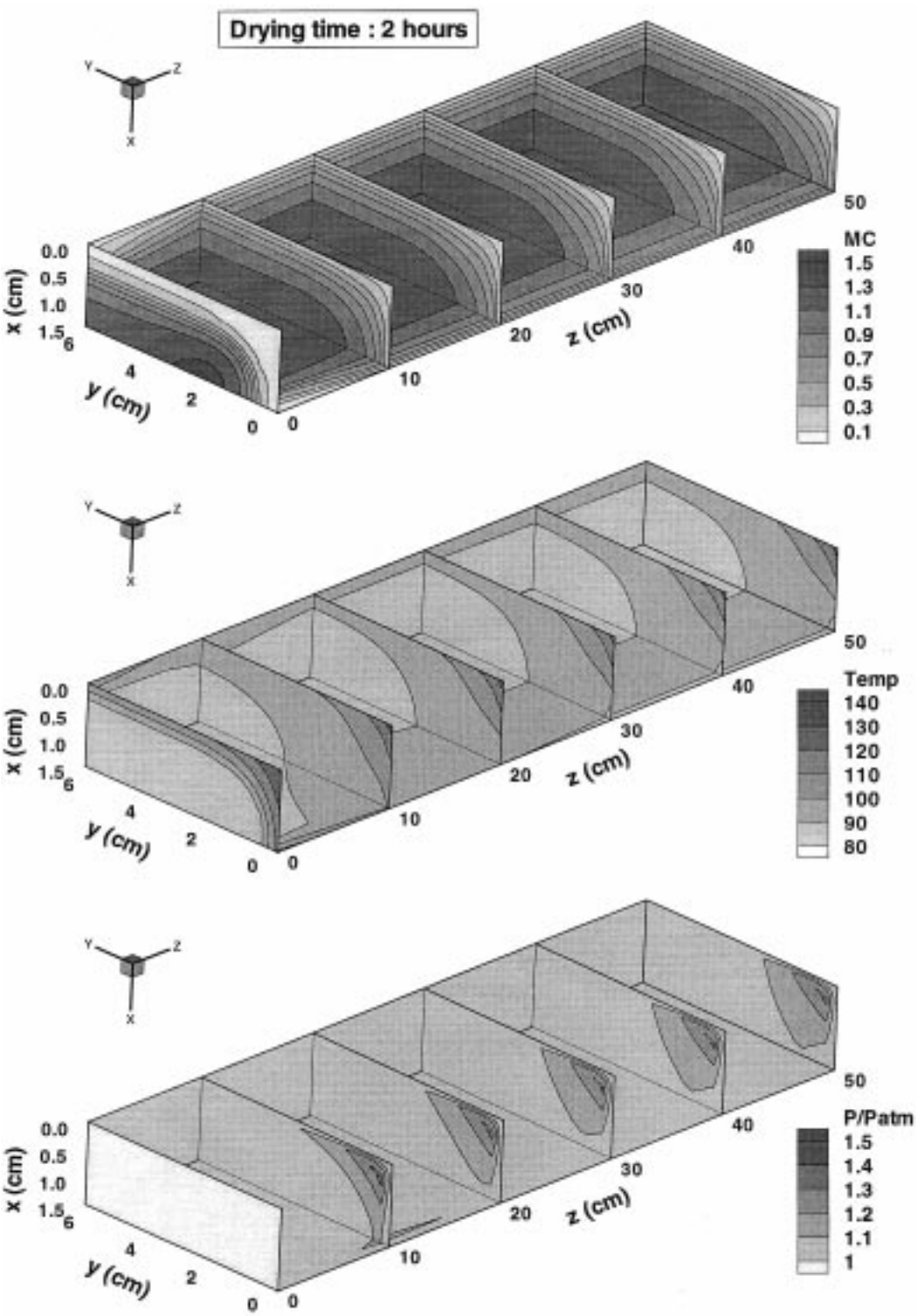

Fig. 9. High temperature drying of softwood ($T_{dry} = 140°C$, $T_{wet} = 80°C$). Fence plot of moisture content, temperature and dimensionless pressure at 2 h of drying.

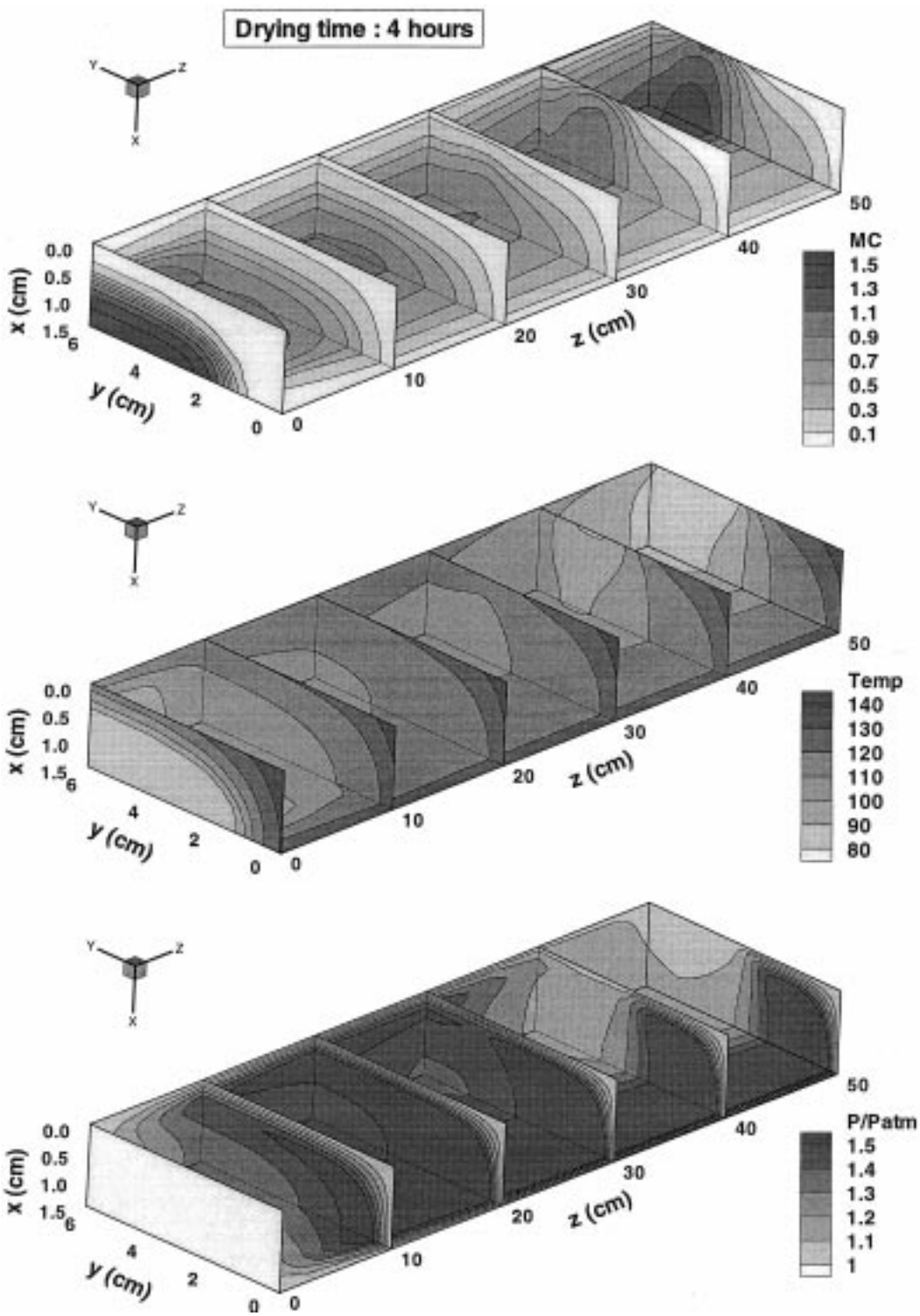

Fig. 10. High temperature drying of softwood ($T_{dry} = 140°C$, $T_{wet} = 80°C$). Fence plot of moisture content, temperature and dimensionless pressure at 4 h of drying.

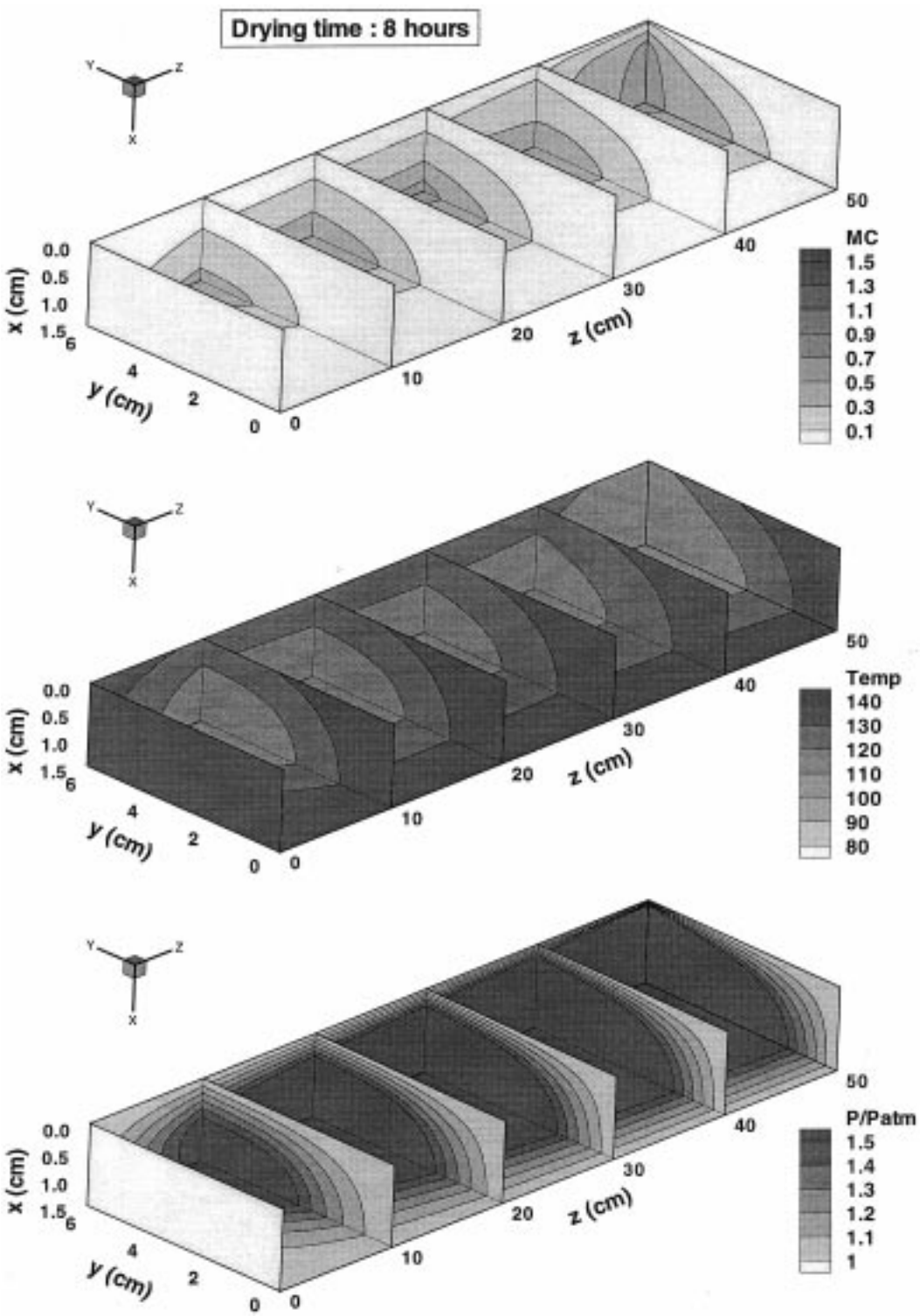

Fig. 11. High temperature drying of softwood ($T_{dry} = 140°C$, $T_{wet} = 80°C$). Fence plot of moisture content, temperature and dimensionless pressure at 8 h of drying.

temperature field is very close to a uniform field at the dry bulb temperature.

By perfectly insulating one or two faces, 2- or 1-D configurations have also been computed (infinite width, infinite length and both). The results are reported as time evolutionary curves of the global moisture content and centre pressure (Fig. 8).

To main remarks can be made from an analysis of these curves:

- the evolution of centre pressure is affected only by the state of the endpiece (whether it is insulated or not). This is a consequence of the high permeability value in the longitudinal direction;
- the global drying curve depends mainly on the presence of the lateral exchange face. The possibility of transfer at the endpiece has a limited effect on the drying curve.

Although no 2-D configuration is able to account for a full 3-D geometry, the effect of longitudinal transfer has little effect on the moisture field in the half-length section and hence, on the stress field in this section. In conclusion, it remains reasonable to compute this low temperature configuration using a 2-D model that calculates the half-length section. This is particularly true if one is interested by mechanical degrade during drying.

3.3. High temperature convective drying of a board of softwood

Using the same board as for the previous test, a high temperature configuration has been computed (dry bulb temperature = 140°C, dew point = 80°C, heat transfer coefficient = 25 W m^{-2} °C^{-1}).

The simulation results for the 12 cm wide board are depicted at 2, 6 and 12 h of drying in Figs. 9–11, respectively. At 2 h of drying, it can be seen that almost the entire board is within the constant drying rate period. The moisture content decreases gradually from the centre towards the exchange surface. Although perceptible, the longitudinal moisture gradient remains quite low as a direct consequence of the very strong anisotropy factor for the permeability (10^3). Further, the temperature of the board rests at the wet bulb and the gaseous phase extension, produced by the decrease in water content, reduces the internal pressure below the atmospheric pressure. All of these mechanisms have been widely analysed in previous research (see for example [10]). What is more interesting here is the edge effect, which is a direct artefact of the third spatial dimension. Due to the presence of two orthogonal exchange faces, the moisture content decreases much faster at the edge of each section. Consequently, this part of the board is already in the second drying period, with a very localised temperature increase. The effect of this phenomenon on the pressure also can be observed all over the length of the board near this corner. The consequence of this slight overpressure is a wet zone that can be seen at the endpiece exchange face, close to the edge.

As the process continues, the zone, which is currently in the second drying rate period, extends towards the half-width. As a consequence, a corresponding zone with overpressure also develops, giving rise to an important water migration mechanism in the longitudinal direction, towards the endpiece of the board. This phenomenon causes the fully saturated zone to enlarge at the end of the board at the location that corresponds with the longitudinal projection of the zones where liquid is available and, where an overpressure exists. This coupled transport mechanism forces this phenomenon to manifest at the mid-thickness quite close to the later exchange surface and to extend progressively towards the mid-width as the overpressure becomes sufficient at the centre. Fig. 10 (4 h of drying) illustrates these intricate mechanisms perfectly. Due to the large increase in temperature initiated at the corner, a zone with a large overpressure exists near the board boundary. Note the endpiece wetting that now appears at the centre of the section.

Another interesting phenomenon appears at the mid-length of the board. Due to the increase in temperature, and hence, in pressure that came from the edge, an important pressure gradient existed within this section for a long period, driving the moisture from the edge towards the half-width. The corresponding wet zone is clearly shown on the 50 cm section (moisture field in Fig. 10). As a consequence of this high moisture content, free water exits at the surface that keeps the temperature close to the wet bulb temperature. The coupling between transfer mechanisms is so that this low temperature enhances the pressure gradient, which in turn causes this state to continue.

This very particular coupling is consistent with the physical phenomena and physical properties embedded within the model. In fact, this phenomenon does not appear to depend on the mesh size and has even been observed in 2-D computations within an R–T section [17]. Nevertheless, this mechanism seems to be sensitive to the values of the physical parameters and the drying conditions. To our knowledge, it has never been reported in the literature. Nevertheless, it is worth noting that the endpiece re-saturation and its effect on the temperature have been studied in detail as a direct consequence of the results that were predicted at first by the 2-D version of TransPore [21]. Consequently, in our opinion, this numerical observation needs to be verified experimentally in the near future.

As the process evolves, this liquid zone finally vanishes and the entire endpiece enters the hygroscopic range (Fig. 11, 8 h of drying). Thereafter, the coupled

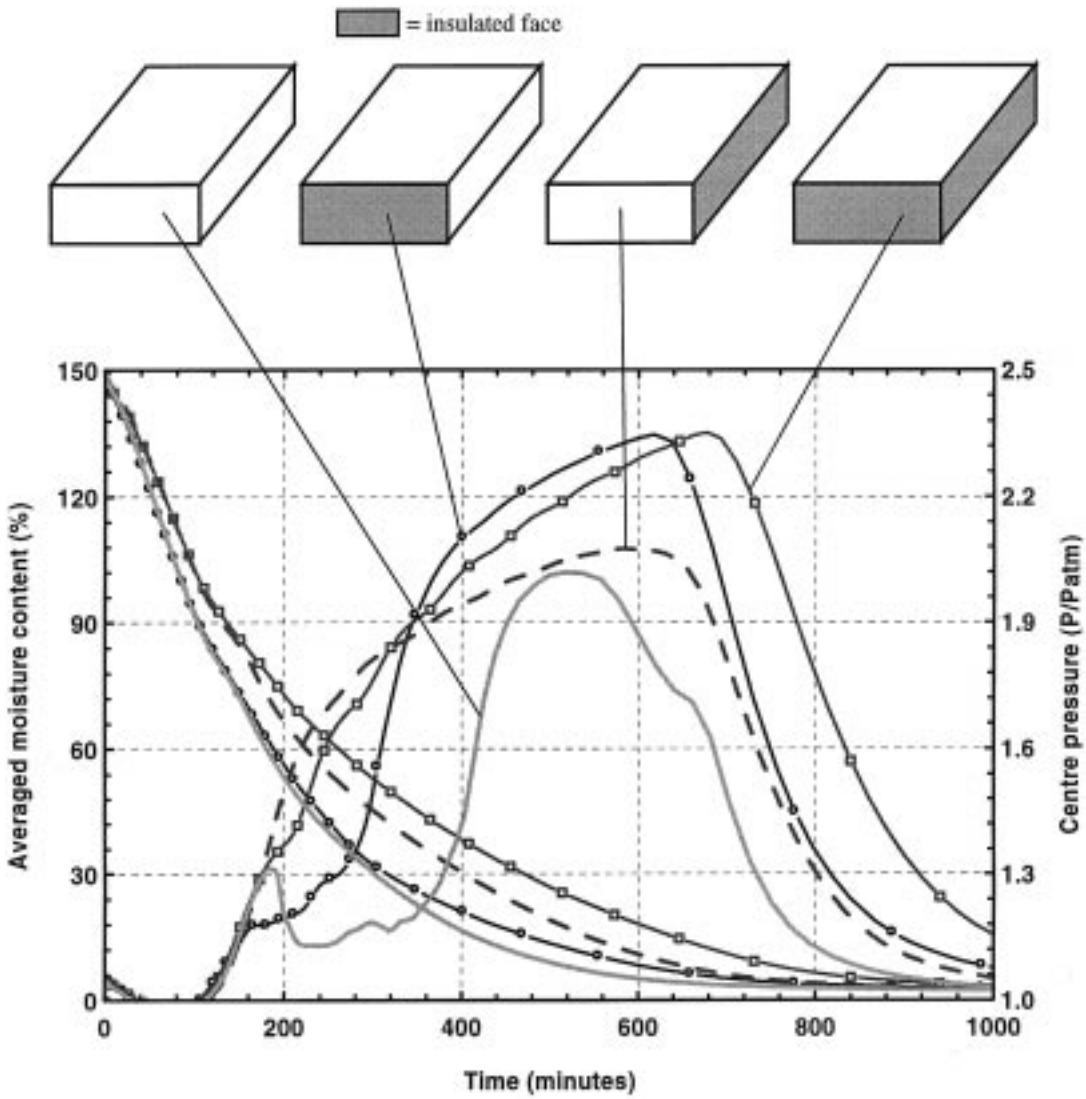

Fig. 12. High temperature drying of softwood ($T_{dry} = 140°C$, $T_{wet} = 80°C$). Overall drying curve and internal pressure for different configurations of exchange surfaces.

mechanisms are not as pronounced and the variable gradients have almost the same sign whatever the coordinate axes. Temperature decreases from the exchange faces towards the centre, regardless of direction. Moisture content decreases from the centre towards the exchange faces, as does the pressure field. Note that some signs of the previous effect can be detected on the temperature and moisture content fields plotted at 50 cm.

The process is now moving towards its end. Energy is driven within the board due to heat conduction, liquid water evaporates inside the medium and moisture moves out of the board due to diffusion (vapour and bound water) as well as advection (Darcy's law applied to the gaseous phase).

2-D or 1-D configurations have also been computed (infinite width, infinite length and both). The results are reported in the form of a time evolution of global moisture content and centre pressure (Fig. 12).

It is evident from the pressure curves that the re-saturation of the surface at mid-length and mid-width exists only when exchange is possible from the lateral face. This is the condition for the pressure gradient to drive liquid towards the centre of the piece. The phenomenon is enhanced and lasts for 200 min when longitudinal migration exists (full 3-D model). A

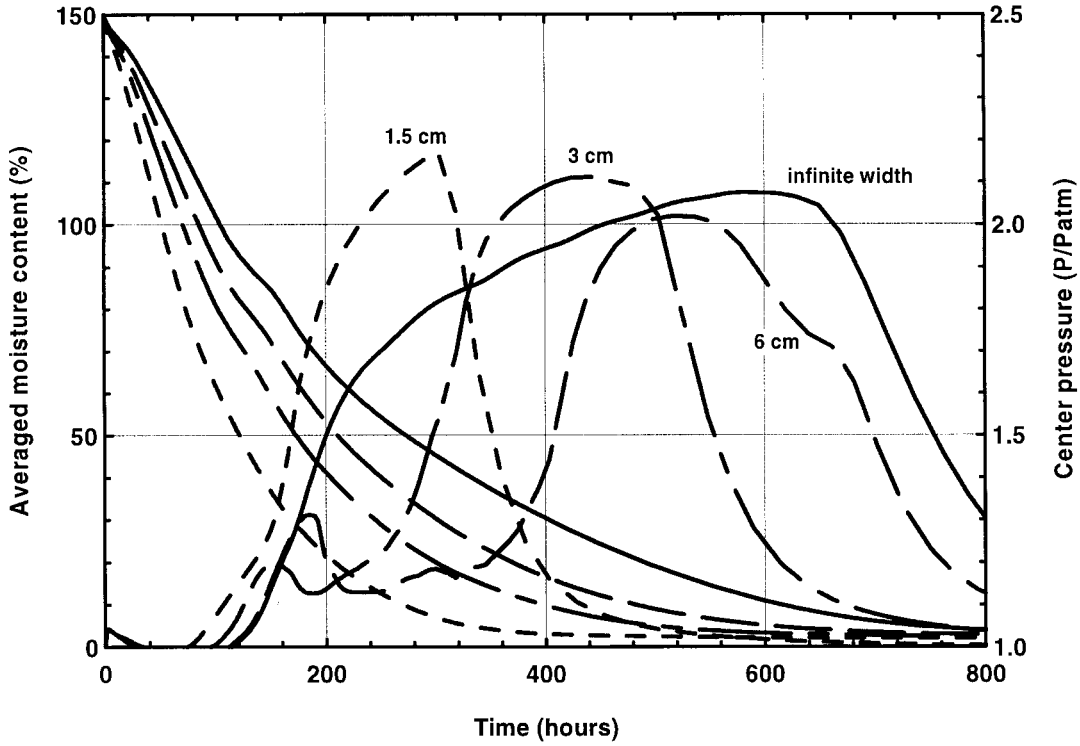

Fig. 13. Overall drying curve and internal pressure for different widths.

detailed analysis of all curves proves that any change of the face status changes the global behaviour of the process:

- the evolution of centre pressure is always affected by any change in the exchange faces;
- although the global drying curve depends mainly on the presence of the lateral exchange face, the possibility of transfer in the longitudinal direction has, through Darcy's law, a significant effect for this high temperature configuration. This result confirms the well-known behaviour of wood during drying with internal vaporisation.

For this case of high temperature drying, no 2-D configuration is able to account for the full 3-D geometry. The lateral face is important in terms of drying rate, while the endpiece has an important effect on the pressure field, hence, on the mechanisms involved throughout the entire sample. In conclusion, the use of any 2-D configuration imposes a quite coarse assumption concerning drying.

From this previous analysis of transfer mechanisms, the three-dimensional aspects of drying have been well exhibited. This is particularly obvious for an anisotropic material such as wood. Our last figure better depicts the effect of board width upon the overall drying process (Fig. 13). An infinite width corresponds to a 2-D simulation for L- and T-directions.

As expected, the drying process is as fast as the board width is small. In the range of 8 to 20% of the final moisture content, the total drying time varies by a factor of 2 to 3 between a square section and an infinite width. In addition, a closer observation of the curve reveals an interesting fact: the constant drying rate period, which is obvious for the infinite section, almost disappears for the square section (the drying curve is never a straight line, even during the first instants of drying). This is a consequence of the presence of the edges, which shift very quickly to the falling drying rate period. It is very important to notice that this shape of the displayed curves corresponds with experimental observation.

Two comments concerning the centre pressure:

- the pressure levels seems to depend only slightly on the board width. However, their shapes can be different and are not simply scaled in time according to the process duration as was the case for the isotropic material;
- during the falling rate period, the increase in temperature from the corner gives rise to a zone with high pressure. As previously explained, a pressure gradient is generated not only from this zone towards the surface, but also from this zone towards

the middle of the section. The latter is responsible for a liquid supply towards the centre of the board that exists only in the case of 3-D transfer. From the evolution of the centre pressure, it can be seen that two conditions must exist for this phenomenon to appear:

(i) the lateral face is not insulated;
(ii) the board width is higher than the board thickness.

This observation is consistent with the mechanisms that were used to explain the process earlier: non-uniform heating of the section from the edge zone that enters at first in the second drying period.

4. Conclusions

For the first time, a drying model that is able to deal with a comprehensive set of macroscopic equations in three spatial dimensions has been presented. Bearing in mind that treating the third dimension produces large computational meshes, which in turn leads to a dramatic increase in computational effort, numerous up-to-date numerical strategies have been implemented in order to allow the code to simulate the drying process efficiently. The present version of TransPore allows a complete simulation of the convective drying of either an anisotropic or isotropic porous medium, dried under severe external conditions, within a few hours on a classical Personal Computer. Regarding the increasing computer power, this computation time is more than reasonable.

The physical analysis presented in this paper highlighted the ability of this code to be closer to reality than every before. Typical 3-D phenomena have been captured and exhibited for each of the given case studies that are unable to be obtained using the current 2-D theory.

The new 3-D version of TransPore appears to be a very promising tool for improving and furthering the understanding of the drying process. Our future aim is to validate the results predicted by the model using experimental data and to use the computation model for the simulation of dielectric drying and vacuum drying operations, as well as for the calculation of drying stresses. These particular drying processes are typical examples for which the third dimension is of utmost importance.

Acknowledgements

One of the authors, Ian Turner, would like to thank the French organisation INRA for funding his visit to the ENGREF/INRA laboratory to enable this work to be realised. The travel assistance offered under the Personal Development Program at the QUT should be also acknowledged.

Appendix A. Physical values used in the simulation

A.1. Physical properties for light concrete

For this medium, results are available in terms of liquid migration for steady state experiments [23]. The liquid migration coefficient, names a_{m1}, defined in this way is connected to the capillary pressure by the following equation

$$\rho_0 \bar{\bar{a}}_{m1} = \rho_l \frac{\bar{\bar{K}}_l \times \bar{\bar{k}}_l}{\mu_l} \frac{\partial P_c}{\partial X}$$

In previous works, the liquid migration coefficient was calculated as follows:

$$\log_{10}(\rho_0 a_{m1}) = \sum_{i=0}^{5} a_i X^i$$

with $a_0 = -10.5$; $a_1 = 30.54$; $a_2 = -70.75$; $a_3 = 83.97$; $a_4 = -49.92$; $a_5 = 11.88$.

Due to the Newton–Raphson formulation, it is more consistent to deal with a capillary pressure curve. This allows the effects of capillary pressure and total pressure to be treated together as a liquid pressure gradient. A capillary pressure curve has been derived in accordance with the expression of a_{m1} together with the relative permeability curve of the liquid phase.

Material properties	Values used for the computations
Porosity	0.80
Density of solid matrix	500 kg m^{-3}
Heat capacity	$\overline{\rho C_p} = \rho_0(840 + 4185X)$ (J kg^{-1} °C^{-1})
Irreducible moisture content	$X_{irr} = 0.07$
Sorption isotherm	If $X \leq X_{irr}(P_v/P_{vs}) = (X/X_{irr}) \times [2-(X/X_{irr})]$ Else $P_v = P_{vs}$
Thermal conductivity	$\lambda_{eff} = 0.142 + 0.46 \times X$ (W m^{-1} °C^{-1})

Capillary pressure	$P_c = 40 \times \sigma \times \exp(8.4057 \times 10^{(-0.3476 X_{wf})})$
Gaseous diffusion	$D_{\text{eff}} = 0.2 \times D_v \times k_{rg}$ D_v is the mass diffusivity of vapour in the air phase
Intrinsic permeability	2×10^{-13} m^2

Liquid moisture content	Relative permeability of the liquid phase	Relative permeability of the gas phase
$X \leq X_{\text{irr}}$	0	1
$0 \leq S_{fw} \leq 1$ with $S_{fw} = \max\{0, [(X - X_{\text{irr}})/(X_{\text{sat}} - X_{\text{irr}})]\}$	$(S_{fw})^3$	$1 + (2S_{fw} - 3)(S_{fw})^2$

A.2. Physical properties for softwood

Because wood is highly hygroscopic, bound water has to be separated from free liquid:

$$X = X_b + X_{fw}$$

where

$$X_b = \min(X_{fsp}, X)$$

and

$$X_{fsp} = 0.325 - 0.001T \quad (\text{at full saturation}, X_{\text{sat}} = X_{fsp} + X_{fw\ \max})$$

The saturation variable involved in the relative permeability functions is calculated according to the free water content only:

$$S_{fw} = \frac{X_{fw}}{X_{fw\ \max}}$$

Scalar values Material properties	Values used for the computations
Porosity	0.67
Density of solid matrix	500 kg m^{-3}
Heat capacity	$\overline{\rho C_p} = \rho_0(1113 + 4.85T + 4185X)$ (J kg^{-1} K^{-1})
Sorption isotherm	$(P_v/P_{vs}) = 1 - \exp(-0.76427A - 3.6787A^2)$ with $A = X_b/X_{fsp}$
Capillary pressure	$P_c = 1.364 \times 10^5 \sigma (X_{fw} + 1.2 \times 10^{-4})^{-0.61}$

Tensorial values Material direction	Tangential	Radial	Longitudinal
Gaseous diffusion	$D^T_{\text{eff}} = 10^{-3} \times k_{rg} \times D_v$	$D^R_{\text{eff}} = 2 \times D^T_{\text{eff}}$	$D^L_{\text{eff}} = 100 \times D^T_{\text{eff}}$
Bound water diffusion	$D^T_b = \exp[-9.9 - 9.8X_b - (4300/T_k)]$	$D^R_b = 2 \times D^T_b$	$D^L_b = 2.5 \times D^T_b$
Thermal conductivity	$\lambda^T_{\text{eff}} = 0.142 + 0.46 \times X$	$\lambda^R_{\text{eff}} = 2 \times \lambda^T_{\text{eff}}$	$\lambda^L_{\text{eff}} = 2 \times \lambda^T_{\text{eff}}$
Intrinisc liquid permeability	1×10^{-15} m^2	2×10^{-15} m^2	1×10^{-12} m^2
Intrinsic gas permeability	1×10^{-16} m^2	2×10^{-16} m^2	1×10^{-13} m^2
Liquid relative permeability	$k^T_{rl} = (S_{wf})^3$	$k^R_{rl} = k^T_{rl}$	$k^L_{rl} = (S_{wf})^8$
Gaseous relative permeability	$k^T_{rg} = 1 + (2S_{wf} - 3)(S_{wf})^2$	$k^R_{rg} = k^T_{rg}$	$k^L_{rg} = 1 + (4S_{wf} - 5)(S_{wf})^4$

References

[1] K. Aziz, A. Settari, Petroleum Reservoir Simulation, Academic, New York, 1979.

[2] N. Boukadida, Nasrallah S. Ben, Two-dimensional heat and mass transfer during convective drying of porous media, J. Drying Technology 13 (3) (1995) 661–694.

[3] F. Couture, P. Fabrie, J-R. Puiggali, An alternative choice for the drying variables leading to a mathematically and physically well described problem, J. Drying Technology 13 (3) (1995) 519–550.

[4] P.A. Forsyth, R.B. Simpson, A two phase, two component model for natural convection in a porous medium, Int. J. Numer. Methods Fluids 12 (1991) 655–682.

[5] P.A. Forsyth, Three-dimensional modelling of steam flush for DNAPL site remediation, Int. J. Numer. Methods Fluids 19 (1994) 1055–1081.

[6] C. Fyhr, A. Rasmuson, Numerical simulation of superheated steam drying of wood chips, in: V. Rudolph, R. Keey, A.S. Mujumdar (Eds.), Drying 94, Proceedings of the 9th International Drying Symposium, Gold Coast, Australia, 1994, pp. 727–734 (Part B).

[7] H. Mounji, J. Bouzon, Absorption and desorption of water in a wood beam, below and above the fiber saturation point, with three-dimensional diffusion, Holzforschung 46 (5) (1992) 439–447.

[8] P. Perré, D. Maillet, Drying of softwoods: the interest of a two-dimensional model to simulate anisotropy or to predict degrade, in: 2nd IUFRO International Wood Drying Symposium, Seattle, USA, 1989, pp. 226–237.

[9] P. Perré, A. Degiovanni, Simulations par volumes finis des transferts couplés en milieu poreux anisotropes: séchage du bois à basse et à haute temperature, Int. J. Heat and Mass Transfer 33 (11) (1990) 2463–2478.

[10] P. Perré, I. Turner, The use of macroscopic equations to simulate heat and mass transfer in porous media, in: I. Turner, A.S. Mujumdar (Eds.), Mathematical Modeling and Numerical Techniques in Drying Technology, Marcel Dekker, New York, 1996.

[11] P. Perré, I.W. Turner, Microwave drying of softwood in an oversized waveguide, AIChE Journal 43 (10) (1997) 2579–2595.

[12] P. Perré, I.W. Turner, TransPore: a generic heat and mass transfer computational model for understanding and visualising the drying of porous media. Invited paper to appear in J. Drying Technology, 1999.

[13] H. Petersson, O. Dahlblom, S. Ormarsson, K. Persson, Moisture distortion modelling of wood and structural timber, in: Proceedings of the International Conference of COST Action E8, Copenhagen, Denmark, 1997, pp. 173–195.

[14] P.H. Sammon, An analysis of upstream weighting, Soc. Petrol. Eng. J. Res. Eng. 3 (1988) 1053–1056.

[15] B. Sleep, J. Skyes, Compositional simulation of groundwater contaminants by organic compounds 1. Model development and verification, Water Resources Res. 29 (1993) 1697–1708.

[16] I. Turner, P. Perré, A synopsis of the strategies and efficient resolution techniques used for modelling and numerically simulating the drying process, in: I. Turner, A.S. Mujumdar (Eds.), Mathematical Modeling and Numerical Techniques in Drying Technology, Marcel Dekker, New York, 1996.

[17] I.W. Turner, P. Perré, The use of implicit flux limiting schemes in the simulation of the drying process: a new maximum flow sensor applied to phase mobilities, submitted to the Journal of Applied Mathematical Modelling, 1998.

[18] S. Whitaker, Simultaneous heat, mass, and momentum transfer in porous media: a theory of drying, Advances in Heat Transfer 13 (1977) 119–203.

[19] S. Whitaker, Coupled transport in multiphase systems: a theory of drying, Advances in Heat Transfer 31 (1998) 1–104.

[20] P.R. Forsyth, Three-dimensional modelling of stream flush for DNAPL site remediation, Int. J. Numerical Methods Fluids 19 (1994) 1055–1081.

[21] P. Perré, M. Moser, M. Martin, Advances in transport phenomena during convective drying with superheated steam or moist air, Int. J. Heat Mass Transfer 36 (11) (1993) 2725–2746.

[22] H.A. van der Vorst, Bi-CGSTAB: a fast and smoothly converging variant of Bi-CG for the solution of nonsymmetric linear systems, SIAM J. Sci. Stat. Computat. 13 (1992) 631–645.

[23] O. Krischer, K. Kröll, Techniques du séchage, CETIAT, Orsay, 1963 (translation of the original text published in 1956: Dir Wissenschaflichen Grundlagen der Trocknungstechnik, Springer Verlag).